MAGNETIC
RESONANCE
IMAGING

Magnetic resonance imaging of alternating electric currents

Urša Mikac, Franci Demšar, Katarina Beravs, Igor Serša*

Jožef Stefan Institute, Ljubljana, Slovenia

Abstract

Electric Current Density Imaging (CDI) is a new modality of magnetic resonance imaging that enables electric current distribution imaging in conductive samples containing water. So far, two CDI techniques have been in use: DC-CDI operating at zero frequency and RF-CDI operating at the RF Larmor frequency. In this paper we present a new CDI technique, which extends the CDI frequency range to alternating electric currents (AC-CDI). First, a theoretical model for the electric current response to the alternating voltage is presented. Later, this model is used for the frequency analysis of the AC-CDI sequence. Additionally, the effect of off-resonance spins and imperfect refocusing RF pulses on the stability of the AC-CDI sequence and the echo formation is studied. The new theory is verified by experiments on a model system and compared to the other two methods: DC-CDI and RF-CDI. Finally, an application of the AC-CDI sequence to biological systems is demonstrated by an experiment on a wood twig in which an increase of approximately 30% was obtained at AC as compared to DC electric current. © 2001 Elsevier Science Inc. All rights reserved.

Keywords: Electric current density imaging (CDI); Alternating electric currents; Electric conductivity mapping; Electric conductivity in biological systems

1. Introduction

Electric current density imaging (CDI) is a magnetic resonance imaging technique designed to image electric current density in conductive samples containing water. The principle of CDI is based on mapping magnetic field changes caused by electric currents flowing through the sample. Once maps of the magnetic field changes are obtained, the electric current density can be calculated from field change maps using Ampere's law. Early CDI attempts used chemical shift imaging techniques to image constant direct electric currents [1]. Because of the linear relation between the magnetic field and frequency, magnetic field change maps can be easily calculated from the chemical shift images. Later, phase sensitive CDI techniques were developed [2–4] which are based on application of the electric current in pulses to produce temporal shifts of a precession frequency and consequently also phase shifts. These shifts can be added cumulatively by an appropriate arrangement of electric and RF pulses in the CDI sequence and later detected by a phase sensitive MRI.

Existing phase sensitive CDI techniques enable electric current density imaging at two different frequency ranges: at zero frequency using a direct current density imaging technique, DC-CDI [2–6], and at the Larmor frequency using an RF electric current density technique RF-CDI [7,8]. The sensitivity of all CDI techniques is proportional to: the inverse impedance of the sample, the applied voltage, the total duration of all electric pulses, and the signal to noise ratio (SNR) of the conventional MR image [5,6]. Both techniques, DC-CDI and RF-CDI, produce good results on test samples where sample impedance can be set. However, in biologic systems electrical characteristics cannot be changed. The impedance is relatively high at low frequencies and is considerably lower at higher frequencies. Consequently, RF-CDI in biologic systems is much more sensitive and produces better results than DC-CDI. One way to increase DC-CDI sensitivity is to increase the applied voltage. The main problem associated with application of high voltage for in vivo experiments in biologic systems is muscle stimulation. However, successful in vivo DC-CDI experiments have already been reported [9,10]. The impedance in systems, such as electrolytes, is independent of frequency. Unlike biologic systems, no increase in the sensitivity of CDI as a result of moving to higher frequencies is expected in these systems; DC-CDI and RF-CDI give practically the same results.

Two different impedance characteristics have their origin

---

* Corresponding author. Tel.: +386-1-477-3696; fax: +386-1-426-3269.

E-mail address: igor.sersa@ijs.si (I. Serša).

in ionic organization. In electrolytes ions can move freely, whereas in biologic systems, besides extracellular ions (which behave like ions in electrolytes) there are also intracellular ions that are restricted in their motion by cell walls. Ions in electrolytes as well as extracellular ions possess purely resistive characteristics. The decrease of impedance in biologic systems at higher frequencies is due to the capacitive properties of cell membranes [11]. Besides the electric current of extracellular ions, an electric polarization current of intracellular ions also flows within cells whenever the voltage changes.

Many applications may be found where maps of the specific impedances obtained at various frequencies by different CDI techniques can provide better understanding of fundamental physical or biologic processes. CDI applications are mainly in biologic systems; i.e., DC-CDI help in designing and positioning new types of electrodes used in tumor electrochemo-therapy [10,12]. The same technique also can be applied to analysis of ion concentrations in the sample and its dynamics; i.e., DC-CDI monitoring of chemical reactions where ions are released or dissolved [13]. The potassium ion concentration is very important for the condition of wood and a decrease of the concentration may be an indication of a wood disease [14]. Similar applications of DC-CDI can be found also in medicine. The calcium level in the bones of patients with osteoporosis is significantly lower than that of healthy volunteers. Therefore, electric current density images obtained by DC-CDI could help to diagnose osteoporosis [15]. The spinal cord contains thousands of nerve fibers (axons) that conduct electrochemical impulses between the brain and the rest of the body. As such, the DC-CDI technique may be indicative of the current carrying capability of the spinal cord and thus provide a true measure of function and viability of the tissue [16]. In an in vivo DC-CDI experiment currents passing from a rabbit's head to its rear leg were monitored [9]. Not only has DC-CDI been used for applications, but also the first applications of RF-CDI are emerging. An example of this is a study of evoked depolarization in the brain that is present at status epilepticus. In status epilepticus the specific impedance in some regions of the brain are about 10% below normal and can be detected by RF-CDI [17].

In this paper we present a new technique for CDI that enables imaging of alternating electric currents in the kHz frequency range (AC-CDI). AC-CDI operates between two frequency extremes: zero frequency (DC-CDI) and radio frequencies (RF-CDI). It has the advantage of increased sensitivity common to the RF-CDI method and can be performed on the same hardware platform as the DC-CDI method. Similarly to DC-CDI, AC-CDI has also pulses of electric voltage synchronized with the standard spin-echo imaging sequence. Two rectangular electric pulses, which are used for the DC-CDI technique, are in the case of the AC-CDI technique replaced by a train of many shorter rectangular electric pulses with alternating polarity that have the same effect as alternating current. The AC electric

current produces changes in static magnetic field which can be detected by a phase sensitive MRI and later processed in the same way as other phase sensitive CDI techniques.

2. Materials and methods

2.1. Current response to alternating rectangular voltage pulses

We must first examine the current response to an electric voltage step for three typical situations: (a) freely mobile ions in the electrolyte solution (extracellular ions); (b) the electric polarization current of cell membranes (intracellular ions) and (c) the combination of both mechanisms as a model for a biologic system. We assume that the voltage changes at time $t = 0$ from a voltage $(U_0 - \Delta U)$ to U_0. A relationship for mobile ions in electrolytic solutions that can be schematically represented by a resistor R_m (Fig. 1a) is given by

$$I(t) = \frac{U_0}{R_m}. \tag{1}$$

The situation is more complex if ions in the sample cannot move freely, i.e., they are blocked by cell membranes and cannot therefore contribute to the DC electric current. However, upon application of an external electric field (a voltage pulse), electric dipole moments are induced in cell membranes, resulting in electric polarization. The cell therefore behaves as a small capacitor C in series with a resistor R_c (Fig. 1b), where the function of the resistor R_c is to regulate the rate of cell charging and discharging. The corresponding solution for $t \geq 0$ is then

$$I(t) = \frac{\Delta U}{R_c} \exp(-t/(R_c C)). \tag{2}$$

In biologic systems both ion transport mechanisms mentioned above are acting in parallel [11]. Schematically, a biologic sample can be represented by an electric circuit consisting of a resistor R_c and a capacitor C in series (cell membranes) with a shunt R_m representing mobile ions in the extracellular fluid (Fig. 1c). In this case an electric current response to the voltage step for $t \geq 0$ is given by

$$I(t) = \frac{U_0}{R_m} + \frac{\Delta U}{R_c} \exp(-t/(R_c C)). \tag{3}$$

Equations (2–4) allow simple calculation of the current response associated with an alternating electric voltage in rectangular pulses of a duration Δt (with a period $2\Delta t$) and an amplitude U_0. Simulations of the electric current response to the voltage pulse for these three electric schemes are presented in Fig. 1. Parameters for the simulations are: $R_m = R_c = 130 \ \Omega$, $C = 2.2 \ \mu F$, $\Delta t = 2$ ms, and $I_0 = U_0/R_m = U_0/R_c$. The same results can also be obtained by Fourier
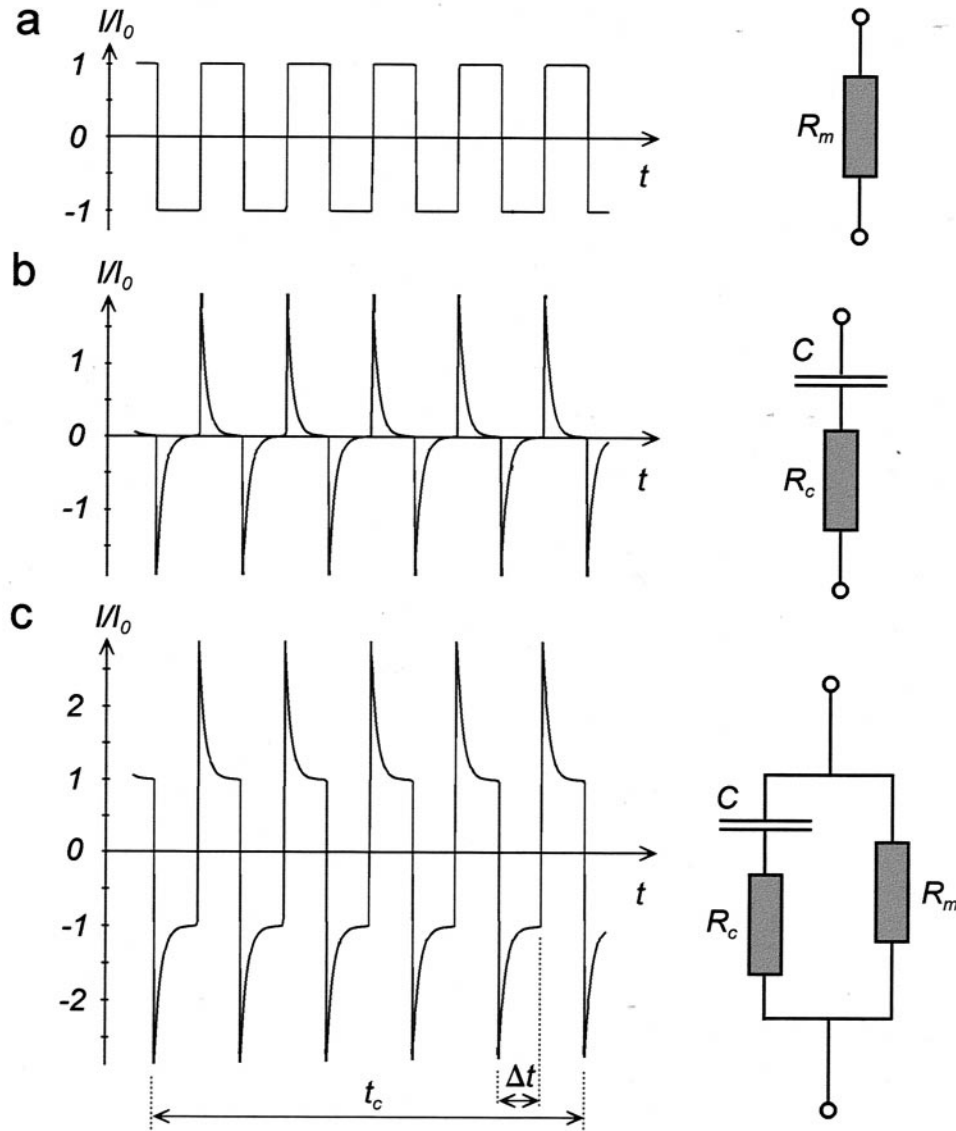
Fig. 1. Electric current response to alternating rectangular voltage pulses for three different electric circuits: (a) a resistor representing mobile extracellular ions, (b) a resistor and a capacitor connected in series representing cell membranes and (c) combination of both as a model for a living system.

decomposition [18] in which the voltage is decomposed to its frequency components $U(\omega)$ by Fourier transform followed by calculation of the electric currents using the relation $I(\omega) = U(\omega)/Z(\omega)$, and concluded with a summation of electric current components at all frequencies (the inverse Fourier transformation). Equation (4) encompasses all of these steps

$$I(t) = \frac{1}{2\pi} \int \frac{1}{Z(\omega)} \left[\int U(t') \exp(i\omega t') \, dt' \right]$$

$$\exp(-i\omega t) \, d\omega. \tag{4}$$

Here, voltage, current and impedance are complex functions. In our case impedances are: $Z(\omega) = R_m$ for freely mobile ions (a), $Z(\omega) = R_c + 1/(i\omega C)$ for a system of cell

membranes (b), and $Z(\omega) = (R_m^{-1} + (R_c + 1/(i\omega C))^{-1})^{-1}$ for the biologic system (c).

2.2. AC current density imaging sequence

To understand the AC (alternating current) Current Density Imaging method (AC-CDI) we must first examine the direct current DC-CDI imaging method [2–4]. DC-CDI is based on a conventional spin-echo MRI sequence on which two rectangular electric pulses are superimposed (Fig. 2a). The first pulse with duration $\Delta t = t_c/2$ is executed between the excitation $\pi/2$ pulse and the refocusing π pulse, while the second current pulse is symmetric to the first one with the same duration but the opposite polarity. Electric current with density $\vec{j}$ that flows through the sample during the pulse alters the static magnetic field $\vec{B}_0$ in the sample by an
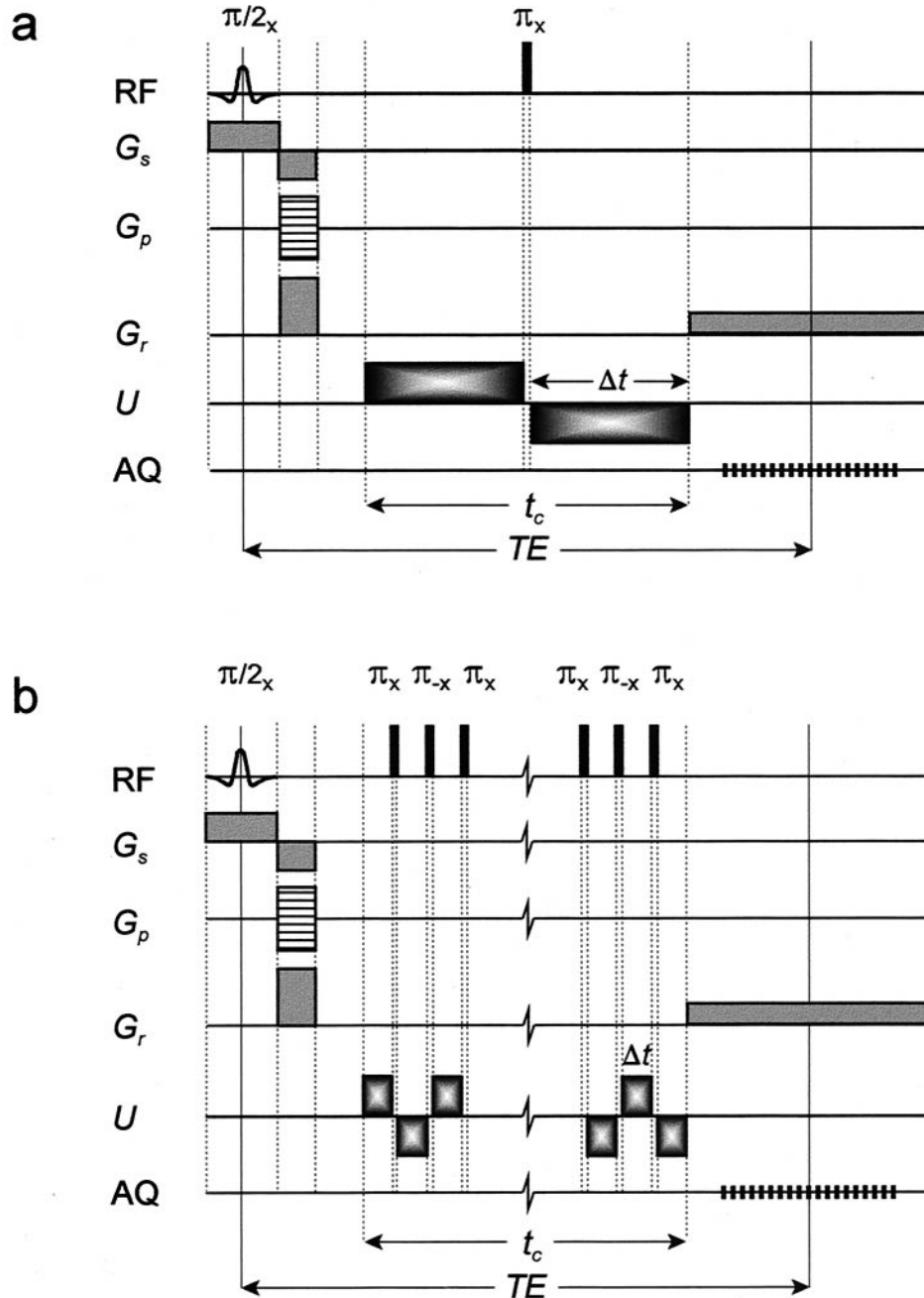
Fig. 2. Direct current density imaging sequence (DC-CDI) (a) and alternating current density imaging sequence (AC-CDI) (b). Both sequences are based on a standard spin-echo imaging sequence with a modified refocusing part: The DC-CDI sequence has two electric pulses of opposite polarity centered around the π pulse, whereas AC-CDI has a block of $(N-1)$ π pulses of alternating phase, which are inserted between N alternating electric pulses. A spin-echo is formed after the AC-CDI sequence only when N is even.

additional field $\vec{B}_c$. The component $B_c \equiv B_{c,z}$, along the direction of the static magnetic field, causes a shift in the Larmor frequency $\omega_c = \gamma B_c$ which results in an accumulated phase shift of $\varphi_c/2 = \gamma B_c \Delta t$. This shift is reversed to $-\varphi_c/2$ after the π pulse and is later added to the phase shift produced by the second electric pulse, which due to the opposite polarity is also equal to $-\varphi_c/2$. The cumulative phase shift of the DC-CDI technique is therefore equal to a sum of both individual phase shifts $-\varphi_c/2 - \varphi_c/2 = -\varphi_c$.

The electric current in the DC-CDI technique is not exactly direct. The two electric pulses of opposite polarity used for DC-CDI may be considered to be a period of alternating electric voltage. A better approximation of the alternating voltage and consequently the alternating electric current through the sample may be obtained by adding many pairs of the pulses together to form a train of alternating rectangular electric pulses. Using the same principle as before for DC-CDI, i.e., insertion of refocusing RF pulses

between each pair of electric pulses of the opposite polarity, enables constructive summation of individual phase shifts. The AC-CDI imaging sequence as shown in Fig. 2b can be therefore considered an extension to the DC-CDI sequence, where the current/RF block is repeated several times, so that the train of alternating rectangular electric pulses is inserted between refocusing RF pulses. An AC-CDI pulse sequence with N electric pulses has N-1 refocusing RF pulses. Each electric pulse except the last one is followed by the refocusing RF pulse. DC-CDI is then a special case of AC-CDI where $N = 2$.

A typical DC-CDI experiment utilizes an electric current supply as a generator for the electric pulses. However, for AC-CDI a current supply is not a good choice, since the electric current through the sample would always be the same no matter what its electrical characteristics, i.e., for all electric schemes in Fig. 1 the same electric current response would be obtained. A more suitable approach is to use an electric voltage supply which applies a constant voltage to the sample during the pulse. In this case, the electric current through the sample is dependent on the sample impedance, and similar electric current responses to those simulated in Fig. 1 may be expected.

If we suppose that the absolute value of a cumulative phase shift after the AC-CDI sequence is equal to $|\varphi_c|$; then the phase shift after the first electric pulse is equal to $|\varphi_c|/N$; after the second, $-2|\varphi_c|/N$; after the third $3|\varphi_c|/N$; ... and after the last (N-th) electric pulse, $(-1)^N |\varphi_c|$. Therefore, the phase shift after the AC-CDI imaging sequence is given by the equation

$$\varphi_c = (-1)^{N-1} N \int_0^{t_c/N} \gamma B_c(t) \, dt$$

$$= (-1)^{N-1} \gamma \langle B_c \rangle \, t_c, \qquad (5)$$

where $\Delta t = t_c/N$ is a duration of one electric pulse. The electric current in the AC-CDI experiment is not constant within the electric pulse causing the phase shift after the pulse $|\varphi_c|/N$ to be proportional to the average magnetic field change $\langle B_c \rangle$ of the pulse multiplied by its duration $\Delta t = t_c/N$. In Eq. (5), it is also assumed that all electric current pulses produce the same phase shift but this is not exactly true. Namely, at the first pulse, the voltage rises from 0 to U_0 and then drops from U_0 to 0 after the last pulse. At all the other pulses, the voltage rises or drops by $2U_0$. This effect does not influence the electric current of freely mobile ions, which is the same at all electric pulses. However, it influences the electric polarization current which flows anytime the voltage changes and is proportional to this change (Figs. 1b,c). The electric polarization current that occurs at the first pulse is half of that of other pulses, which follows also from Eqs. (3, 4). Namely, the voltage change at the first pulse is equal to $\Delta U = U_0$ and equals $\Delta U = \pm 2U_0$ at all other pulses. Also, the electric polarization current flows with half the magnitude after the last electric pulse. Since there is no refocusing RF pulse at the end of the last electric pulse in the AC-CDI sequence, the phase shift produced by this current cancels with the phase shift of the first pulse.

The procedure to calculate a current density image is the same as in DC-CDI [2–4]. For example, to obtain an image of a current density component j_z in the xy plane two maps of magnetic field changes in the xy plane are required: $\langle B_{c,x} \rangle$ and $\langle B_{c,y} \rangle$. Each of them is calculated using relation $\langle B_c \rangle = \varphi_c/(\gamma \, t_c)$ [Eq. (5)] from a corresponding phase shift map φ_c of the sample in one of two orientations that are 90° apart around the direction of the electric current component in question (z axis). It should be noted that indexes x, y and z denote the axes of the coordinate system attached to the sample and not to the laboratory reference system in which the z direction is reserved for the direction of the static magnetic field B_0. Therefore, a $\langle B_{c,x} \rangle$ map is measured for a sample orientation with the x axis aligned to B_0 and similarly a $\langle B_{c,y} \rangle$ map is measured for a sample orientation with the y axis aligned to B_0. Finally, the average electric current density within the electric pulse (effective current) $\langle j_z \rangle$ is calculated using Ampere's law $\langle \vec{j} \rangle = 1/\mu_0 \nabla \times \langle \vec{B}_c \rangle$. In this case, its 2D equivalent can be used

$$\langle j_z \rangle(x,y) = \frac{1}{\mu_0} \left(\frac{\partial \langle B_{c,y} \rangle(x,y)}{\partial x} - \frac{\partial \langle B_{c,x} \rangle(x,y)}{\partial y} \right). \qquad (6)$$

2.3. Refocusing properties of AC current density imaging sequence

The main difference between multi-echo sequences [19–21] and the AC-CDI sequence is in the timing between RF pulses. The time between successive π pulses is not twice the time between the excitation $\pi/2$ pulse and the first π pulse as in multi-echo sequences but usually much shorter. Because of that difference, spin-echoes are not formed between π pulses: the only spin-echo is formed at the end of the sequence when the number of π pulses in the AC-CDI sequence is odd (N is even). Besides the main spin-echo, many stimulated echoes and "eight-ball" echoes [19] are also excited when tip angles of RF pulses in the AC-CDI sequence are imperfect. However, their amplitude is significantly lower than the amplitude of the main echo (provided that tip angle deviations are not too large) and therefore may be neglected in further analysis.

The effect of tip angle deviations, off-resonance spins, and electric current on the spin-echo formation and the accuracy of the electric current phase shift registration can be analyzed by a mathematical model. In this model each event in the AC-CDI sequence is represented by a corresponding rotational matrix. The final magnetization vector can be then calculated as a product of these matrices multiplied by the initial magnetization vector. The proposed AC-CDI sequence is based on the Carr-Purcell multi-echo sequence [20] using a phase alternation of successive π pulses. An alternative would be to use the same phase arrangement as in the Meiboom-Gill multi-echo sequence [21]. The AC-CDI sequence can be schematically represented by
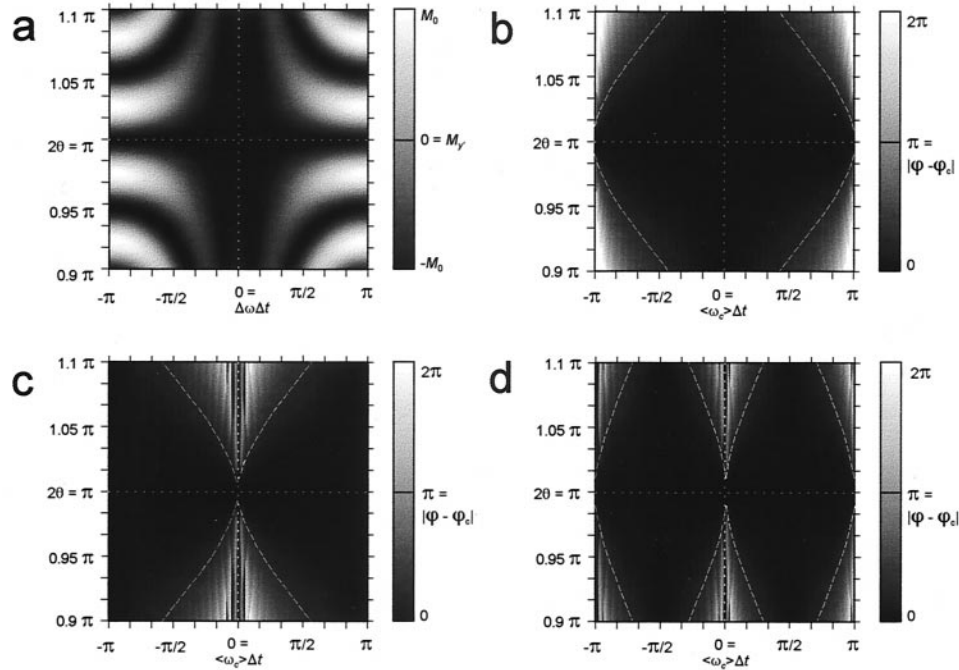
Fig. 3. Simulations of the spin-echo stability (a) and errors in the registration of the magnetic field change of applied electric pulses (b, c, d). The simulated gray-scale image (a) depicts magnetization component $M_{y'}$ at the echo point of the AC-CDI sequence ($N = 40$, $\Delta t = 500$ μs, $TE = 32$ ms, $<B_{c,z}> = 0$) as a function of the off-resonance frequency $\Delta\omega$ and the refocusing pulse tip angle 2θ. The solid line corresponds to the perfect spin-echo conditions at $2\theta = \pi$, when all magnetization components at different off-resonance frequencies are perfectly refocused. Errors in the registration of the magnetic field change (b, c, d) are represented by the absolute difference $|\varphi - \varphi_c|$ between the measured phase shift φ from the image and the cumulative phase shift of electric pulses φ_c, as a function of the effective current magnetic field change $<B_{c,z}>$ and the refocusing pulse tip angle 2θ. The errors are simulated (with parameters $N = 40$, $\Delta t = 500$ μs, $TE = 32$ ms) for: (b) the AC-CDI sequence; (c) the modified AC-CDI sequence based on the Meiboom-Gill multi-echo sequence ((b) and (c) are both simulated for spins on-resonance); and (d) the AC-CDI sequence for spins off-resonance for $\Delta\omega/2\pi = 100$ Hz. Dashed lines plotted in (b, c, d) correspond to a $|\varphi - \varphi_c| = \pi/4$ phase error.

$$\theta_x - t_e - U_0^+ - 2\theta_x - U_0^- - 2\theta_{-x} - U_0^- - \ldots$$
$$- 2\theta_x - U_0^- - t_d - AQ, \qquad (7)$$

where $\pi/2$ and π tip angles are replaced by general tip angles, θ and 2θ, and the excitation time t_e and detection time t_d (measured to the center of the acquisition) are equal to $t_e = t_d = (TE - t_c)/2$. We assume that in a small region of the sample the excitation tip angle is equal to θ, the refocusing tip angle to 2θ, that all spins are off-resonance for exactly $\Delta\omega$, and that each electric pulse shifts the magnetization vector phase by $<\omega_c>\Delta t$, where $<\omega_c> = \gamma <B_{c,z}>$, as defined in Eq. (5). Using these assumptions and Eq. (7), the magnetization vector in the rotating frame after the AC-CDI sequence can be represented by the following sequence of rotations

$$\vec{M} = R_z(\Delta\omega t_d) R_z((\Delta\omega + (-1)^N\langle\omega_c\rangle)\Delta t)$$
$$R_x((-1)^{N-1}2\theta) \ldots R_z((\Delta\omega - \langle\omega_c\rangle)\Delta t)$$
$$R_x(2\theta) R_z((\Delta\omega + \langle\omega_c\rangle)\Delta t) R_z(\Delta\omega t_e)$$
$$R_x(\theta) \vec{M}_0. \qquad (8)$$

Here R_x, R_y, R_z denote rotational matrices with the axis of rotation around the -x, -y and -z axes respectively (indexes x, y, and z correspond to the direction of the magnetic field

which rotates the magnetization, whereas the rotational vector is antiparallel to the magnetic field). The arguments are angles of rotation and $\vec{M}_0$ is the equilibrium magnetization.

The simulation in Fig. 3a depicts the stability of a spin-echo of the AC-CDI sequence as a function of tip angle deviations. The stability is analyzed by a magnetization component $M_{y'}$ at the center of the echo which is calculated from Eq. (8) with parameters: $N = 40$, $TE = 32$ ms, $\Delta t = 500$ μs and without electric pulses ($<\omega_c> = 0$). As expected, the magnetization refocusing is perfect when tip angles of refocusing pulses are ideal; $2\theta = \pi$. For all off-resonance spins then $M_{y'} = -M_0$. As tip angle deviations increase and the magnetization between successive refocusing pulses starts to fan out with larger angles ($|\Delta\omega\Delta t| \approx \pi$), the echo becomes unstable. The magnetization $M_{y'}$ can then in principle be anywhere between $-M_0$ and M_0 depending on the tip angle 2θ (Fig. 3a). The phase coherence between different off-resonant spins is then lost and the magnitude of the spin-echo reduced. However, when $|\Delta\omega\Delta t| \ll \pi$ and $2\theta \neq \pi$, the magnetization $M_{y'}$ is still well refocused ($M_{y'} \approx -M_0$). For off-resonance cases with $|\Delta\omega\Delta t| > \pi$, $M_{y'}$ is symmetrical around $\Delta\omega\Delta t = \pm \pi$ and also periodic with a period $\Delta\omega\Delta t = 2\pi$.

It is important to understand how tip angle deviations influence the accuracy of a measured phase shift map and

consequently the accuracy of a calculated electric current density image. Namely, the cumulative phase shift of applied electric pulses, $\varphi_c = \langle \omega_c \rangle t_c$ [Eq. (5)] cannot be measured directly but is assumed to be equal to a measured phase φ calculated from the real and imaginary signal components of the image. However, that is not exactly true, since the phase φ depends not only on the electric current frequency shift $\langle \omega_c \rangle$, but also on the refocusing pulse tip angle 2θ and the off-resonance frequency $\Delta\omega$ [Eq. (8)]. In general, the phase φ is not equal to the cumulative phase shift of applied electric pulses φ_c, and therefore the measured electric current density images may be inaccurate.

Simulations in Figs. 3b-d depict the absolute error of the measured phase ($|\varphi\text{-}\varphi_c|$) as a function of the average current density (measured in units of the frequency offset $\langle \omega_c \rangle$) and the refocusing pulse tip angle 2θ. Here, φ is the angle between the transverse magnetization $\vec{M}_{x'y'}$ and the $-y'$ axis (y' axis in Fig. 3c) which is calculated from Eq. (8). Other parameters for the simulation are: $N = 40$, $TE = 32$ ms, $\Delta t = 500$ μs. A dashed line is plotted in each simulation identifying the $|\varphi\text{-}\varphi_c| = \pi/4$ error line. In all cases, when refocusing pulses are ideal ($2\theta = \pi$), the phase error is equal to zero (the dark region centered around $2\theta = \pi$). As deviations from the ideal tip angle increase and spins are well on-resonance ($\Delta\omega\Delta t = 0$), the error also increases, however, not equally for the AC-CDI sequence (Fig. 3b) and a modified AC-CDI sequence which is based on the Meiboom-Gill multi-echo sequence [21] (Fig. 3c). The AC-CDI sequence has low error at low electric currents and considerably higher error at higher currents (Fig. 3b). Just the opposite is the situation for the Meiboom-Gill AC-CDI sequence where the error is quite substantial at low electric currents and is practically zero at currents such that $|\langle \omega_c \rangle \Delta t| \approx \pi$. When spins are off-resonance, the error distribution is different. In Fig. 3d, where $\Delta\omega\Delta t = \pi/2$, errors are high when $|\langle \omega_c \rangle \Delta t|$ approaches either 0 or π. Since electric currents are usually low and the spins are on-resonance, so that $|\langle \omega_c \rangle \Delta t| \ll \pi$ and $\Delta\omega\Delta t \approx 0$, a better choice is to use the Carr-Purcell AC-CDI sequence than the Meiboom-Gill modification of it.

3. Results

3.1. Experiments on a model system

Imaging of alternating electric current by the AC-CDI technique was tested on a phantom sample, consisting of two concentric cylinders separated by an insulating wall. The inner cylinder, 4 mm in diameter, was filled with conducting saline (6%) and closed with electrodes on both sides, so that the electric current was flowing along the cylinder axis. The electrodes were 13 mm apart and were connected to a voltage amplifier with output voltage 12 V. The two return wires connecting the electrodes with the amplifier were oriented along the direction of the static

magnetic field. The magnetic field of the return wires was perpendicular to the static magnetic field and therefore did not contribute to the cumulative phase shift of the applied electric pulses φ_c. The outer cylinder, 10 mm in diameter, was used as a reference and was also filled with saline, but had no current flowing through it. The electric current flowed only through the inner cylinder, which had a DC resistance $R_c = 130$ Ω. A capacitor with a capacitance $C = 2.2$ μF was connected in series to the inner cylinder. The sample was inserted in the magnet with its axis perpendicular to the direction of the static magnetic field. Experiments were performed on a 2.35 T Bruker Biospec scanner (Bruker Medizintechnik GmbH, Ettlingen, Germany) equipped with micro-imaging accessories. The AC-CDI technique was tested on a series of micro-images of the phantom sample acquired at different numbers of electric pulses $N = 2$ (DC-CDI), 4, 6, 8, 10, 20, 40 while keeping the total duration of electric pulses constant ($t_c = 20$ ms). These results were also compared to the RF-CDI technique [7,8] with the same duration of the RF pulse (equal to $t_c = 20$ ms) and the same voltage amplitude. Other imaging parameters were: $FOV = 15$ mm, field of view, $SLTH = 5$ mm, slice thickness, 256 by 256, matrix dimensions, $TR = 1$ s, repetition rate and $TE = 32$ ms, echo time. The results of the AC-CDI experiments are shown in Fig. 4 with the images of a real signal component (left), the calculated images of the effective electric current density (middle) and the measured electric current response through the sample (right). As expected from the theory [Eq. (3)], the current response to the train of alternating electric pulses for a sample, which can be electrically described by a series RC circuit (Fig. 1b), corresponds to a train of exponentially decaying alternating signals of electric current. Each rectangular voltage pulse produces a signal with an effective electric current equal to the area below the signal divided by Δt (also the average electric current over a pulse). Simulation of the electric current response to the rectangular alternating voltage in Fig. 1b, which was calculated for the same parameters as were used in the experiment ($R_c = 130$ Ω, $C = 2.2$ μF, $t_c = 20$ ms, and $N = 10$), agrees well with the measured electric current response in Fig. 4 ($N = 10$, right). The only differences are in the heights of the first and the last signals, which are halved due to the half voltage raise of the first pulse and the half voltage drop after the last pulse.

If we suppose that the sample is oriented so that the cylinder axis is along the z axis, then $\vec{B}_0$ is along the y axis and the imaging plane is xy. For a uniform electric current I within the inner cylinder of the sample, the magnetic field change $B_{c,y}$ is given by

$$B_{c,y}(r,\Phi) = \frac{\mu_0 I}{2\pi a} \begin{cases} \dfrac{r}{a}\cos(\Phi); & r \leq a \\[2mm] \dfrac{a}{r}\cos(\Phi); & r > a \end{cases}. \qquad (9)$$
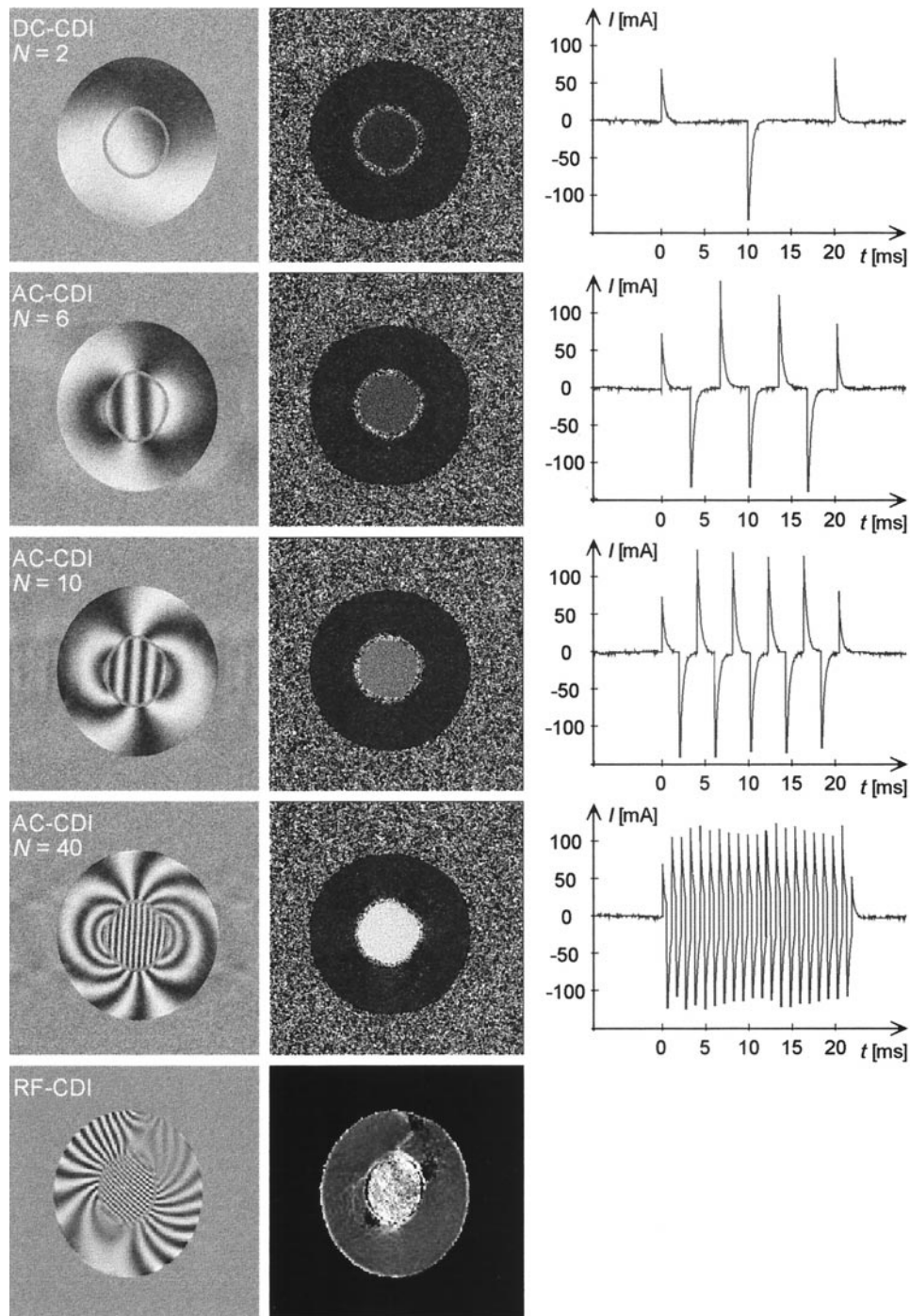
Fig. 4. Electric current density micro-images of a cylindrical phantom sample in axial orientation acquired at different frequencies of electric pulses (DC, 150 Hz, 250 Hz, 1 kHz, and RF at 100 MHz): real signal component images (left), calculated current density images (middle) and the measured electric current response to electric pulses of the AC-CDI sequence (right). The phantom sample consists of two cylinders filled with saline, an isolated outer cylinder and a conductive inner one. The inner cylinder was also connected in series to the external capacitor. The images were acquired with parameters: $FOV =$ 15 mm, field of view, $SLTH = 5$ mm, slice thickness, $TR = 1$ s, repetition rate, $TE = 32$ ms, echo time, and $t_c = 20$ ms, total duration of electric pulses. The increasing brightness of the inner cylinder in the calculated current density images (middle) indicates that the effective electric current increased as the frequency of electric pulses increased. The same may be concluded also from the measured electric current response (right) as well as from the real signal component images (left), where the patterns of alternating bright and dark stripes are more intense as frequency increases.

Here, r and Φ are polar coordinates defined by $x = r \cos(\Phi)$ and $y = r \sin(\Phi)$ and a is the radius of the inner cylinder. Since phase shifts φ_c are proportional to the magnetic field change $B_{c,y}$, lines of constant phase are defined by

$r \cos(\Phi) = x = constant$ inside the inner cylinder (lines parallel to $\vec{B}_0$) and by $1/r \cos(\Phi) = constant$ outside it (circles tangential to the y axis with centers on the x axis). Alternating dark and bright stripes in the real signal com-

ponent images (Fig. 4, left) correspond to regions of constant phase. These regions match the constant magnetic field lines in and outside the cylindrical conductor calculated above. There is always a 2π phase difference between two successive dark or bright stripes. Therefore, a denser pattern of stripes corresponds to a higher gradient of the phase φ_c, and hence also to a higher current density.

Two maps of magnetic field change: $<B_{c,x}>$ and $<B_{c,y}>$ are needed for calculation of the electric current density $<j_z>$ in the xy plane [Eq. (6)]. Normally, this would imply sample rotation of 90° around the z axis in order to acquire $<B_{c,x}>$ and $<B_{c,y}>$ maps, each in one orientation. However, the phantom sample had cylindrical symmetry so that the two phase shift maps, which are used to calculate corresponding magnetic field maps, would be the same. Therefore, only one phase shift map φ_c was used to calculate both $<B_{c,x}>$ and $<B_{c,y}>$. The map $<B_{c,y}>$ was calculated directly from the phase shift map φ_c (assuming that $\vec{B}_0$ was oriented along the y axis), whereas map $<B_{c,x}>$ was calculated from the rotated phase shift map φ_c for a 90° clockwise rotation. Finally, the effective current density $<j_z>$ was calculated using the Eq. (6). Gray-scale images of the effective electric current density in Fig. 4 (middle) have 256 gray levels with the brightest level corresponding to the current density of 7000 A/m^2 and the darkest to the current density of -1000 A/m^2. The electric current was flowing only through the inner cylinder and no electric current was flowing through the outer one.

In our experiment, the effective electric current through the sample increased with the frequency of the voltage pulses, i.e., with increasing N at fixed t_c. This was due to the decrease of the impedance of the sample (series R_cC) with increasing frequency. This is evident from real signal component images (Fig. 4, left) as well as from the current density images (Fig. 4, middle). The real signal component images have a denser pattern of stripes, while the current density images have an increasing signal within the inner cylinder indicating a higher effective electric current density at higher N's. As long as the current decay rate (R_cC constant) of the circuit with equivalent electrical characteristics to the phantom sample is shorter than the duration of the electric pulse Δt, the increase of the effective electric current density is approximately proportional to the number of electric pulses N. In our case R_cC was equal to 290 μs, hence, it was always less than the electric pulse duration (at $N = 40$ was $\Delta t = 500$ μs). The above condition was therefore met for all frequencies used in the AC-CDI experiment in Fig. 4. However, at RF currents (Fig. 4, last row) the increase of the effective electric current density is not proportional to the frequency increase, since Δt is much shorter than the R_cC constant of the sample. The effective electric current density at a radio frequency of 100 MHz increased by approximately 50% compared to the effective electric current density at 1 kHz ($N = 40$), whereas the frequency increased by a factor 10^5. It should also be noted that for a current source, as opposed to a voltage source, the
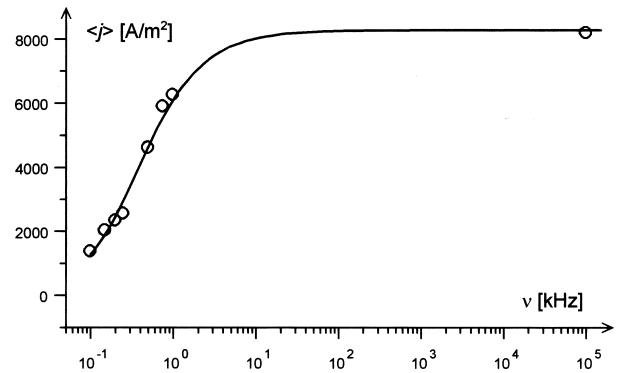

Fig. 5. The effective electric current density as a function of the electric current frequency: a computer simulation (solid line) based on the theoretical model [Eq. (4)] and experimental data (circles) drawn from Fig. 4. The effective electric current increases with the frequency of electric pulses until the plateau at the frequency $1/(R_cC)$.

effective electric current would be constant independent of the frequency of electric pulses.

A graph in Fig. 5 depicts the dependence of the effective electric current density $<j>$ on the frequency ($\nu = 1/(2\Delta t) = N/(2t_c)$) of the electric current which was measured in the experiment on a model system. Experimental results are also compared with the results of the theoretical model based on the electric circuit with a resistor and a capacitor connected in series (Fig. 1b). Equation (2) together with the relation $<j> = \int_0^{\Delta t} I(t)dt/(\pi a^2 \Delta t)$ was used to calculate the theoretical effective current density (solid line in the graph). As expected, the increase of the effective electric current density $<j>$ is linear for frequencies lower than $1/(R_cC)$ (3.5 kHz), whereas for frequencies higher than $1/(R_cC)$, the plateau at $<j> = U_0/(\pi a^2 R_c)$ occurs.

3.2. AC-CDI technique on a biologic sample

A wood twig of the elder-tree (*Acer negundo L.*) with a diameter 15 mm and length 13 mm was selected for a demonstration of the AC-CDI technique on a biologic sample. The twig was inserted into a plastic holder which ended with electrodes on both ends. These were connected to the voltage amplifier with an output voltage of 85 V. The twig was then inserted into the magnet with its axis perpendicular to the direction of the static magnetic field. To calculate the z component of the effective electric current density ($<j_z>$), the twig was imaged at two perpendicular orientations 90° apart around the z axis: one with its x axis in the direction of the static magnetic field and the other with its y axis in this direction, so that maps of the magnetic field change $<B_{c,x}>$ and $<B_{c,y}>$ were acquired and used later to calculate $<j_z>$ using Eq. (6).

Two images of the effective electric current density: one with DC electric current ($N = 2$, $\Delta t = 10$ ms) and the other with AC electric current at 1 kHz ($N = 40$, $\Delta t = 500$ μs), were acquired in order to demonstrate the decrease of the impedance with a frequency increase. Other imaging pa-
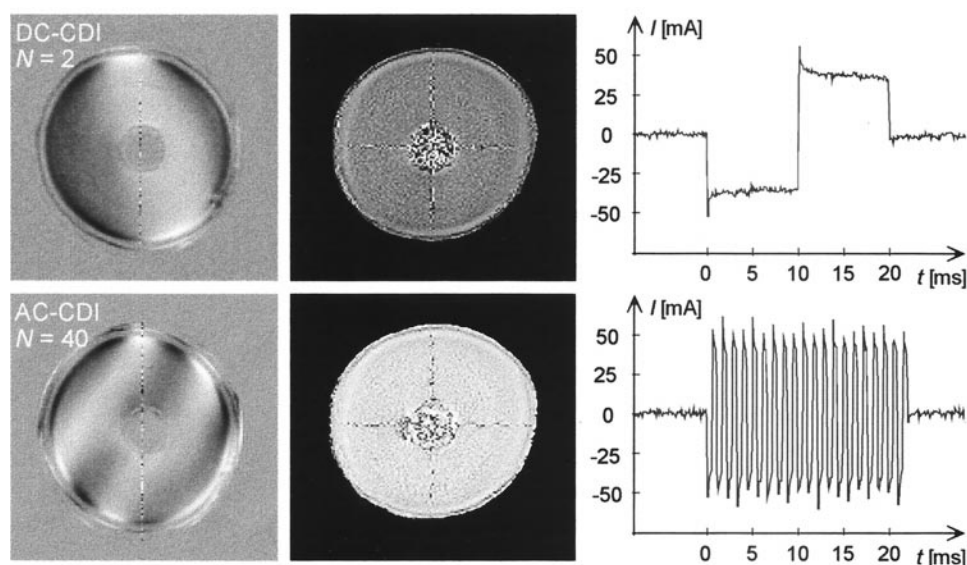
Fig. 6. DC and AC (at 1 kHz) current density images of a wood twig in an axial orientation: real signal component images (left), calculated current density images (middle) and the measured electric current response to electric pulses of the AC-CDI sequence (right). The images were acquired at parameters: $FOV = 20$ mm, field of view, $SLTH = 5$ mm, slice thickness, $TR = 600$ ms, repetition rate, $TE = 32$ ms, echo time, $t_c = 20$ ms, total duration of electric pulses, and $U_0 = 85$ V, the applied voltage. Background noise in current density images is removed. Note the approximately 30% increase of the effective electric current density in *xylem* (dominating region surrounding pith) with the AC-CDI technique as compared to the DC-CDI technique.

rameters were: $FOV = 2$ cm, field of view, $SLTH = 5$ mm, slice thickness, $TR = 600$ ms, repetition rate, $TE = 32$ ms, echo time, and $t_c = 20$ ms, total duration of electric pulses. Fig. 6 shows the experimental results of the DC-CDI technique (first row) and the AC-CDI technique (second row) on the wood twig. Each experiment is presented with a real signal component image (left), a calculated current density image (middle) and an electric current time dependence (right). The gray-scale images of the effective electric current density have 256 gray levels which correspond to electric current densities from $<j_z> = 0$ A/m^2 (image intensity 0) to $<j_z> = 350$ A/m^2 (image intensity 255).

As can be seen from Fig. 6, the electric current density is not uniform through the cross-section of the twig for both CDI techniques: DC and AC. This is due to different specific impedances of different wood tissues [22]. Besides having different specific impedances at a certain frequency, each tissue has different specific impedances at different frequencies. This can be seen also in our demonstration. The wood twig consists of the following tissues appearing in concentric rings from the outside toward the center: bark, cambial zone, xylem, and pith. Bark appears dark in the DC-CDI as well as in the AC-CDI image due to its high specific impedance. Unlike bark, cambial zone and xylem have considerably lower specific impedances, so the electric current densities in these two regions are relatively high. However, the effective electric current density is not the same for the DC-CDI and AC-CDI techniques due to the decrease of the specific impedance with the increase of frequency. For example, in the dominating xylem region, this decrease was approximately 30% with the effective electric current density in xylem in the DC-CDI experiment

equaling 190 A/m^2 but it increased to 250 A/m^2 in the AC-CDI experiment at 1 kHz. The same effect can be seen also from the real signal component images which have at AC electric current more black and white stripes indicating a higher effective electric current density in this region. In pith the current density cannot be determined because of insufficient NMR signal. The decrease of impedance can be also estimated from the electric current response to alternating voltage pulses as shown in Fig. 6, right. Namely, the maximum increase is equal to the ratio between the electric current peak at the electric pulse beginning where both, extracellular and intracellular ions conduct, and the current at the electric pulse end, where the response is flat and only ions in extracellular fluid conduct. This ratio was in our experiment 50 mA to 33 mA, which corresponds to a maximum decrease of impedance of approximately 40%.

3.3. Discussion and conclusions

The technique for imaging alternating electric currents (AC-CDI) presented here fills the gap in the frequency range between the techniques for imaging direct electric currents (DC-CDI) and radio-frequency electric currents (RF-CDI). Even though all three techniques use the same principle to encode and calculate the electric current distribution, they have different fields of use. For example, the DC-CDI method can detect only the electric current associated with the transport of freely mobile ions making it convenient for electrolytic systems where all ions are mobile. The advantage of such electrolytic systems is that sample resistance can be arbitrarily set to the desired value, so that a low resistance needed for a typical DC-CDI ex-

periment can be easily obtained. The situation in biologic systems is quite different. Namely, most biologic samples have inherently high resistance (high impedance at zero frequency) which cannot be changed. Therefore, in most cases, the DC-CDI sequence cannot give acceptable results if used with typical parameters. In biologic systems cell membranes act like tiny capacitors which, when charged, block the DC electric current of intracellular ions. As a consequence, only ions in the extracellular fluid conduct.

When a biologic sample is connected to an alternating voltage source, cell membranes change electrical polarization with the frequency of the source. Whenever the polarization is changed, the electric polarization current of intracellular ion flows in addition to the extracellular electric current. Higher frequencies result in higher time average values of the electric polarization current causing the contribution of intracellular ions to the overall electric current to be more significant. In practice this means that the average (absolute) electric current through a biologic sample would increase at higher frequency of the current if the sample is connected to a supply of a constant voltage amplitude. Therefore, the AC-CDI and especially the RF-CDI technique are more convenient for biologic systems than the DC-CDI technique. In biologic samples, the impedance decreases with increasing frequency. At a certain frequency the impedance reaches a minimum, i.e., for a frequency higher than that, no further decrease of impedance is obtained. This frequency depends on the sample geometry, its dielectric properties and its DC resistance. In our experiment on the wood twig, the impedance decreased about 30% when the AC current was 1 kHz instead of DC.

An inconvenience of the DC-CDI technique as well as of the AC-CDI technique is the need for sample rotation in order to obtain all of the information needed for the current density calculation. However, this can be avoided for samples with cylindrical symmetry, since the magnetic field change map in the rotated sample orientation is identical to the original. Another problem, relates to the AC-CDI application to biologic systems where the impedance at AC frequencies around 1 kHz is only 10–30% lower than the DC impedance. Unfortunately, this decrease is still not enough to enable the use of a relatively low voltage (which is common for DC-CDI experiments in electrolytes) in AC-CDI experiments. A tenfold or higher decrease of impedance would be needed. The other way to increase the AC-CDI sensitivity would be to increase the total duration of all electric pulses. However, the duration is limited by the NMR relaxation properties of the sample. Namely, longer total duration of all pulses results in longer echo-times and consequently less signal is detected due to T_2 relaxation. If the amplitude or the cumulative phase shift of applied electric pulses is low then the SNR of calculated CDI images is low [5,6]. Unlike the DC-CDI technique and the RF-CDI technique, the AC-CDI technique allows arbitrary frequency setting of the electric pulses and therefore also the electric current frequency. However, the advantage of the

RF-CDI technique over other two CDI techniques is that it does not require sample rotation to obtain the two perpendicular components of magnetic field change. Besides, at radio frequencies (RF-CDI), the sample impedance is usually considerably lower than at 1 kHz (AC-CDI) or at zero frequency (DC-CDI).

One problem related to the AC-CDI imaging is also the high RF power needed for hard π pulses. In the theoretical model for the AC-CDI sequence it was assumed that the hard π pulses were infinitely short. However, in a real experiment, that is not the case since infinitely short RF pulses would require infinite power from the RF amplifier. Since this power is always limited, hard π pulses have the shortest possible duration, which is inversely proportional to the power of the RF amplifier and the RF probe size. This however also limits the highest possible frequency of the AC-CDI sequence. For example, if the duration of the π pulse is 25 μs and we assume that each electric pulse should be at least ten times longer than the π pulse, then the highest AC current frequency would be approximately $1/(2\Delta t) = 1/(500 \ \mu s) = 2$ kHz. In many systems it is hard to have the π pulse as short as 25 μs, especially for clinical whole body systems. Due to limited RF power, the frequency range of the AC-CDI sequence is also limited to a few kHz or even less (depending on the system).

It is not exactly true that the frequency of the electric current in the AC-CDI sequence with electric pulses of duration Δt is equal to $1/(2\Delta t)$. As a result of Fourier analysis [Eq. (4)], the train of alternating rectangular electric pulses can be decomposed into many frequency components of different amplitudes [18] including a dominating component (the one with the highest amplitude) of a frequency $1/(2\Delta t)$ and many other harmonics with higher frequencies and lower amplitudes. The electric current response to each of these components is different since the response depends on the sample impedance which changes with frequency. Another problem associated with the application of the AC-CDI to biologic systems is RF power absorption in the tissue. Limits posed by the specific absorption rate (SAR) regulations may restrict the use of the AC-CDI sequence and especially its application to humans. The same problem is even more pronounced in the RF-CDI technique where the long RF pulse is needed to encode the RF B_1 field distribution into the image phase [7,8].

In general, in biologic samples, there are two contributions to the electric current: one with its origin in the freely mobile ions and the other in the dielectric properties of cell membranes. AC-CDI uses the arrangement of π pulses such that both electric current components contribute to the cumulative phase shift of the applied electric pulses. Hence, the calculated effective electric current density image corresponds to the average current density of both electric current components within a pulse. However, it is possible to modify the AC-CDI sequence so that only one electric current component contributes to the cumulative phase shift. For example, to obtain the effective electric current

density image of the electric polarization current only, the AC-CDI sequence can be modified by shifting all π pulses for $\Delta t/2$ so that in the middle of each electric pulse there is also a π pulse. Such a sequence has N π pulses and also N electric pulses with alternating polarity. Assuming that $R_c C \ll \Delta t/2$, phase shifts of the electric polarization current of all electric pulses are summed constructively, whereas phase shifts of the extracellular electric current are zero at each electric pulse. It is also possible to design a complementary sequence, in which only the extracellular electric current contributes to the final phase shift. This sequence has only one long electric pulse and one excitation pulse before it.

It is known that in pathologic tissues such as tumors, or in the brain immediately after a stroke, the ratio between bound and free water changes. This change results in different relaxation times [23] and diffusion properties for the tissue [24]. Not only is the ratio between bound and free water changed in pathologic tissue, but also the ratio between intracellular and extracellular ions is changed as well. This difference may be detected by different electric current density imaging techniques (mentioned above) which enable selective measurements of the effective electric current density for different types of electric current charge carriers: mobile extracellular ions, bound intracellular ions or both. From these measurements it is then possible to determine the ratios between concentrations of intracellular and extracellular ions. Alternatively, the same information can be obtained by frequency dependant specific impedance measurements using the AC-CDI technique.

In summary, AC-CDI is a new technique for imaging alternating electric currents in the kHz frequency range that fills the gap between two existing techniques: the DC-CDI technique for imaging direct electric currents and the RF-CDI technique for imaging radio-frequency electric currents at the Larmor frequency. Results of the AC-CDI technique on a phantom sample, electrically equivalent to a series RC circuit, agree well with the theoretically expected decrease of impedance with the increase of the alternating electric current frequency. The same effect was obtained also in a demonstration of the technique on a biologic sample, where the effective electric current density was 30% higher when the sample was connected to an alternating voltage source at 1 kHz than when it was connected to a DC source of the same voltage. From frequency dependent impedance measurements using the AC-CDI technique, an image of the ratio between extracellular and intracellular ions may be obtained. This may have diagnostic potential, since changing ratios between the intracellular and extracellular ion concentrations may be indicative of a pathologic state of the tissue.

Acknowledgments

References

[1] Manassen Y, Shalev E, Navon, G. Mapping of electrical circuits using chemical-shift imaging. *J Magn Reson* 1988; 76:371–4.

[2] Joy ML, Scott G, Henkelman, RM. In vivo detection of applied electric currents by magnetic resonance imaging. *Magn Reson Imaging* 1989; 7:89–94.

[3] Pesikan P, Joy MLG, Scott GC, Henkelman RM. Two-dimensional current density imaging. *IEEE Trans Instrum Meas* 1990; 39:1048–53.

[4] Scott GC, Joy MLG, Armstrong RL, Henkelman RM. Measurement of nonuniform current density by magnetic resonance. *IEEE Trans Med Imaging* 1991; 10:362–74.

[5] Scott GC, Joy MLG, Armstrong RL, Henkelman, RM. Sensitivity of magnetic-resonance current density imaging. *J Magn Reson* 1992; 97:235–54.

[6] Serša I, Jarh O, Demšar F. Magnetic resonance microscopy of electric currents. *J Magn Reson* 1994; 111A:93–9.

[7] Scott GC, Joy MLG, Armstrong RL, Henkelman RM. RF current density imaging in homogeneous media. *Magn Reson Med* 1992; 28:186–201.

[8] Scott GC, Joy MLG, Amstrong RL, Henkelman RM. Rotating frame RF current density imaging. *Magn Reson Me*d 1995; 33:355–69.

[9] Thompson JDM, Joy MLG, Henkelman RM. Current density imaging in rabbit head and chest. In: Book of abstracts: Tenth Annual Scientific Meeting of the Society of Magnetic Resonance in Medicine, 1991:1274.

[10] Serša I, Beravs K, Dodd NJF, Zhao S, Miklavčič D, Demšar F. Electric current density imaging of mice tumors. *Magn Reson Med* 1997; 37:404–9.

[11] Foster KR, Schwam HP. Dielectric properties of tissues and biological materials: a critical review. *Crit Rev Biomed Eng* 1989; 17(1):25–104.

[12] Miklavčič D, Beravs K, Šemrov D, Čemažar M, Demšar F, Serša G. The importance of electric field distribution for effective in vivo electroporation of tissues. *Biophys J* 1998; 74:2152–58.

[13] Beravs K, Demšar A, Demšar F. Magnetic resonance imaging of chemical processes and reactions. *J Magn Reson* 1999; 37:253–7.

[14] Beravs K, Oven P, Serša I, Torelli N, Demšar F. Electric current density imaging of pedunculate oak (*Quercus Robur* L.) Twigs by Magnetic Resonance Imaging. Holzforschung; 1998;52:541–5.

[15] Beravs K, White D, Serša I, Demšar F. Electric current density imaging of bone by MRI. *Magn Reson Imagin*g 1997; 15:909–15.

[16] Bossart EL, Wirth ED, Silver XS, Mareci TH, Blackband SJ, Freeman, AJ. Current density magnetic resonance imaging of excised normal and injured rat spinal cord. In: Book of abstracts: Sixth Scientific Meeting of the International Society for Magnetic Resonance in Medicine. Vol. 1. Berkeley, CA: ISMRM, 1998:197.

[17] Beravs K, Frangež R, Gerkis AN, Demšar F. Radiofrequency current density imaging of kainate-evoked depolarization. *Magn Reson Med* 1999; 42:136–40.

[18] A. Papoulis, Circuits, and Systems, a Modern Approach, Holt, Rinehart, and Winston, Inc., 1980.

[19] Hahn EL. Spin echoes. *Phys Rev* 1950; 80:580–94.

[20] Carr HY, Purcell EM. Effects of diffusion on free precession in nuclear magnetic resonance experiments. *Phys Rev* 1954; 94:630–8.

[21] Meiboom S, Gill D. Modified spin-echo method for measuring nuclear relaxation times. *Rev Sci Instr* 1958; 29:688–91.

[22] James WL. Electrical properties. In: Concise encyclopedia of wood, wood-based materials. Oxford: Pergamon Press, 1989.

[23] Gupta, RK. NMR Spectroscopy of Cells and Organisms, Boca Raton: CRC Press; 1987.

[24] Le Bihan D, Breton E, Lallemand D, Grenier P, Cabanis E, Laval-Jeantet M. MR imaging of intravoxel incoherent motions: application to diffusion and perfusion in neurologic disorders. Radiology 1986: 161, 401–7.